nature COMMUNICATIONS

ARTICLE

Received 19 Jan 2014 | Accepted 22 May 2014 | Published 18 Jun 2014

DOI: 10.1038/ncomms5183

Template-mediated nano-crystallite networks in semiconducting polymers

Sooncheol Kwon[1,2], Kilho Yu[1,2], Kyoungchun Kweon[1,2], Geunjin Kim[1,2], Junghwan Kim[1,2], Heejoo Kim[2,3], Yong-Ryun Jo[1], Bong-Joong Kim[1,2,3], Jehan Kim[4], Seoung Ho Lee[2,3] & Kwanghee Lee[1,2,3]

Unlike typical inorganic semiconductors with a crystal structure, the charge dynamics of π-conjugated polymers (π-CPs) are severely limited by the presence of amorphous portions between the ordered crystalline regions. Thus, the formation of interconnected pathways along crystallites of π-CPs is desired to ensure highly efficient charge transport in printable electronics. Here we report the formation of nano-crystallite networks in π-CP films by employing novel template-mediated crystallization (TMC) via polaron formation and electrostatic interaction. The lateral and vertical charge transport of TMC-treated films increased by two orders of magnitude compared with pristine π-CPs. In particular, because of the unprecedented room temperature and solution-processing advantages of our TMC method, we achieve a field-effect mobility of 0.25 $cm^2 V^{-1} s^{-1}$ using a plastic substrate, which corresponds to the highest value reported thus far. Because our findings can be applied to various π-conjugated semiconductors, our approach is universal and is expected to yield high-performance printable electronics.

[1] Gwangju Institute of Science and Technology (GIST), School of Materials Science and Engineering (SMSE), Gwangju 500-712, Korea. [2] Heeger Center for Advanced Materials (HCAM), Gwangju Institute of Science and Technology (GIST), Gwangju 500-712, Korea. [3] Research Institute for Solar and Sustainable Energies (RISE), Gwangju Institute of Science and Technology (GIST), Gwangju 500-712, Korea. [4] Pohang Accelerator Laboratory (PAL), Pohang University of Science and Technology (POSTECH), Pohang 790-784, Korea. Correspondence and requests for materials should be addressed to H.K. (email: heejook@gist.ac.kr) or to K.L. (email: klee@gist.ac.kr).

Printable electronics, which utilize π-conjugated semiconducting and metallic polymers (π-CPs) as electronic inks, are emerging as a promising technology for the low-cost production of flexible and lightweight devices for use in future ubiquitous devices[1–4]. However, the device performance of π-CPs remains inferior to that of their inorganic counterparts. In contrast to the well-aligned and highly crystalline structure of conventional semiconductors, in which three-dimensional (3D) band-diffusion transport enables high charge-carrier mobility, the charge dynamics in π-CPs are mostly limited by the structure disorder and/or the amorphous portions at the mesoscopic length scale[5–8]. Therefore, the formation of interconnected pathways along the crystallites of π-CPs is desired to ensure highly efficient long-range charge transport in printable electronics.

Because the ultimate advantage of π-CPs is to fabricate devices from solution on top of plastic substrates, inducing interconnected crystallite structures from π-CP solutions at room temperature (RT) is a challenge. Because π-CP chains exhibit a high degree of conformational disorder and weakly interact with each other through van der Waals forces ($<10\,kcal\,mol^{-1}$) in their solution state, amorphous regions and ordered regions are highly likely to statistically coexist in cast π-CP films. The characteristic chain-entangled structure of the amorphous regions hinders the delocalization of the π-electron wave functions in π-CPs. To reduce the amorphous regions and thereby extend the ordered structure of π-CPs, substantial progress has recently been made in the molecular design and fabrication of π-CP films with an impressive field-effect mobility (μ_{FET}) that exceeds $6\,cm^2\,V^{-1}\,s^{-1}$ (refs 9–13). However, the high-T processing (typically, $T\geq 200\,^{\circ}C$) and the rigid substrates of these techniques are critical factors that limit their application to flexible and printable technologies that utilize plastic substrates.

Recent important developments in polymer field-effect transistors (PFETs) with rigid substrates based on mechanical rubbing[14,15] and/or solvent-induced directional solidification[16] using grooved substrates[11,17,18] are not applicable to newer plastic electronics that use flexible and printable techniques. In addition, because these alignment techniques induce enhanced charge transport ($\mu_{FET}\geq 6\,cm^2\,V^{-1}\,s^{-1}$) only in the lateral direction, these one-dimensional anisotropic systems[11–18] limit their general use in plastic electronics, which require not only lateral charge transport as in PFETs but also vertical charge transport as in polymer solar cells[19] and polymer light-emitting diodes[20]. Therefore, prior to this report, no true interconnected pathway of π-CP with 3D network formation from solution at RT had been demonstrated.

In this work, we report the observation of the structural formation of crystallite-fibril nanostructures and interconnected networks in solution-processed π-CP films fabricated using a template-mediated crystallization (TMC) method at RT. By employing a polymer template incorporated with periodically repeating sulphonic acid side-chain groups, such as poly(4-styrene sulphonic acid) (PSS)[21], π-CPs were crystallized along the PSS template to form a microscale fibril structure via polaron formation and electrostatic interaction between π-CPs and the side chain of PSS. Consequently, the template-mediated fibril structures with light doping are physically interconnected with long-range order, leading to 3D percolation networks in the π-CP films. Therefore, the μ_{FET} values of our TMC-treated π-CP films dramatically increased by one or two orders of magnitude compared with those of the pristine π-CPs without any extra treatments. Additionally, because of the well-connected electrical percolation system within the film, our systems exhibit 3D isotropic transport with the same order of improvement along the vertical and lateral directions.

Results

Solution preparation and TMC reaction. The chemical structure of a π-CP (here poly(3-hexylthiophene-2,5-diyl), (P3HT))[22,23] and PSS are shown in Fig. 1a. After preparing two pristine P3HT solutions ($10\,mg\,ml^{-1}$) by dissolution in a chloroform solvent, we added 10 mg of PSS into one of the P3HT solutions and stirred for more than 3 days (see Methods and Supplementary Fig. 1a and Supplementary Note 1 for more details). All of the sample preparation conditions were identical except for the addition of PSS into one of the samples. We subsequently observed that the TMC reaction of P3HT was initiated along the PSS template. Initial evidence of the P3HT crystallization via TMC was observed in the ultraviolet–visible absorption spectra (Fig. 1a), which exhibited a considerable increase in the 0–0 vibronic transition at 600 nm[24] and in the polaron transition at 1,000 nm[25,26] for the PSS-added solution and film samples (that is, P3HT:PSS). We also observed a distinct electron spin resonance (ESR) signal for the P3HT:PSS (1:1 w/w) solution in the dark at RT, whereas no ESR signal was observed in the pristine P3HT and pure PSS solutions (Fig. 1b). The 1,000 nm absorption feature and the ESR signal of P3HT:PSS provide strong evidence of the presence of radical cations (spin 1/2) on P3HT ($P3HT^{+\cdot}$), which are associated with a lattice distortion known as a polaron state[26] (see the chemical structure in the inset of Fig. 1b). We consider the $P3HT^{+}$ cations to be stabilized by the anions of the PSS template via an electrostatic interaction[21,27], resulting in a new fibril microstructure, as evident in the phase-mode atomic force microscopy (AFM) image of the P3HT:PSS films (Supplementary Fig. 1b). To probe the doping mechanism and the presence of electrostatic interaction between P3HT and PSS, X-ray photoelectron spectroscopy (XPS) measurement was performed on the P3HT and P3HT:PSS films, as shown Fig. 1c. The XPS spectra acquired in the sulphur region of the P3HT and P3HT:PSS films were deconvoluted into two doublets. The doublet peaks in the P3HT film (black line, solid) located at 163.9 and 165.1 eV could be assigned to the sulphur of thiophene[27], whereas the doublet peaks in the P3HT:PSS film (blue line, solid) were located at 164.1 and 165.3 eV, indicating that the sulphur of thiophene would be positively charged[27,28]. In addition, comparing the doublet peaks in the pristine PSS film (unionized sulphonic acid group) located at 169.0 and 170.3 eV (Supplementary Fig. 2) revealed that the doublet peaks of the P3HT:PSS film were slightly shifted towards low binding energy at 168.1 and 169.5 eV, as shown in the inset, which are assigned to the ionized sulphonic acid groups ($-SO3^{-}$) of PSS[27]. From the XPS results, we suggest that the P3HT could be protonated to carry a positive charge on sulphur, which would be electrostatically associated with the ionized SO_3^- of PSS.

Formation of crystallite-fibril nanostructure in the P3HT:PSS film. We observed that the P3HT and PSS continued to develop the TMC formation for more than 72 h (Supplementary Fig. 1). To monitor the progress of formation of the TMC nanostructure, we sequentially characterized the nanomorphology of the P3HT:PSS film as a function of time using high-angle annular dark-field scanning transmission electron microscopy (HAADF-STEM) (Fig. 1d). The pristine P3HT did not exhibit any relevant features. Notably, however, we could identify randomly distributed, irregular-shaped dark spots ranging from 50 to 500 nm (after 24 h). An electron dispersive X-ray spectroscopy (EDS) line-profile analysis on the dark region of P3HT:PSS film (after 24 h) revealed that the composition of oxygen is relatively higher compared with that of sulphur, suggesting the presence of insulating PSS because the specific atoms of the P3HT

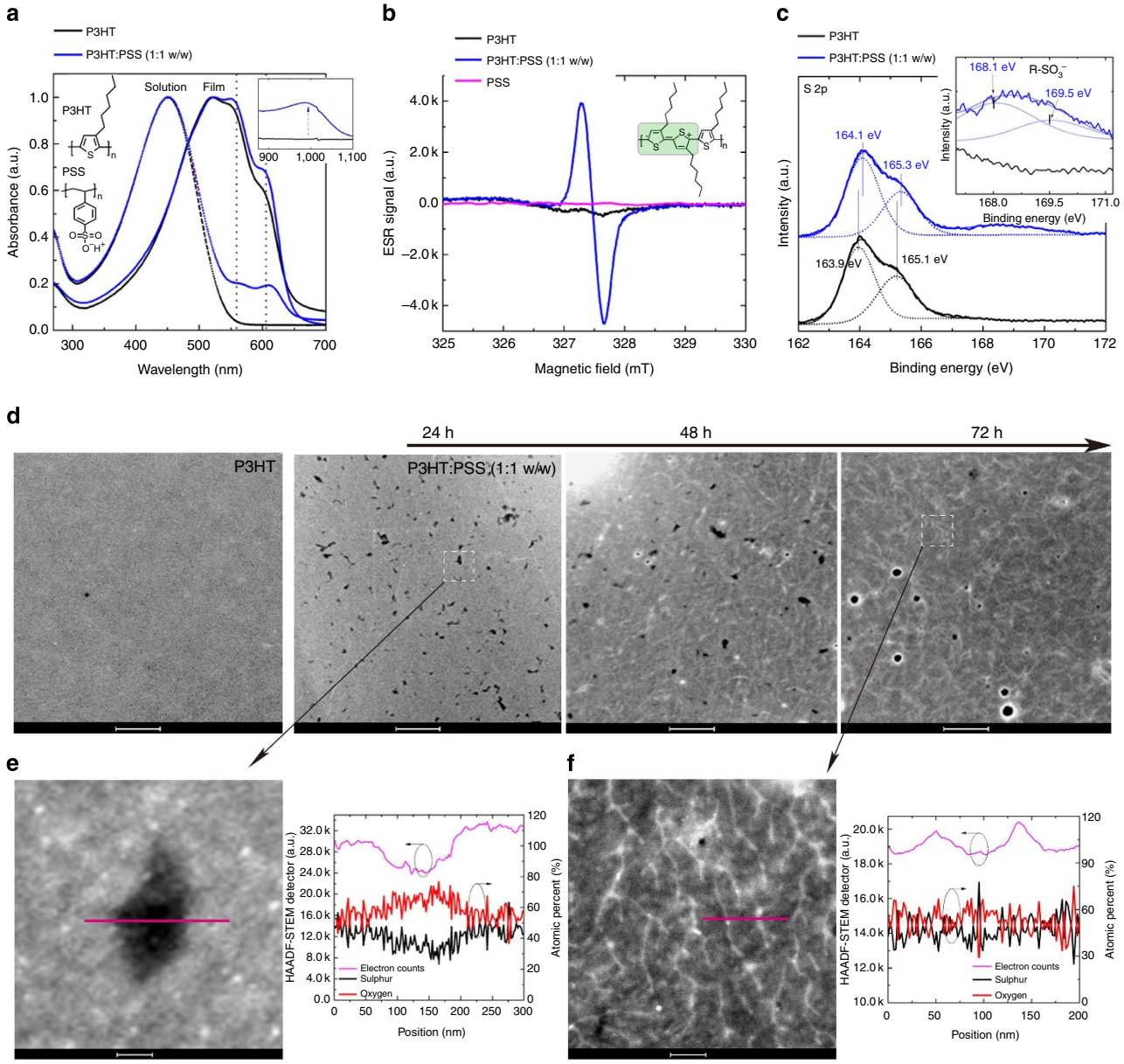

Figure 1 | Characterization of the template-mediated crystallization of P3HT. (**a**) Ultraviolet–visible absorption spectra of the P3HT and P3HT:PSS solutions (dots) and films (solids). The inset presents the absorption spectra at 1,000 nm (1.3 eV), where a polaron transition occurs. (**b**) ESR spectra of the pristine P3HT, PSS and P3HT:PSS solutions. The g-factor is 1.9999. (**c**) X-ray photoemission spectroscopy (XPS) of the corresponding films. The slightly shifted binding energy of sulphur in the P3HT:PSS film (blue line) indicates the presence of positively charged sulphur. The inset reveals the presence of ionized PSS^- in the P3HT:PSS film. (**d**) The sequential change of the nanomorphology of the P3HT:PSS film as a function of time (from 0 to 72 h) using high-angle annular dark-field scanning TEM (HAADF-STEM). Scale bars, 1 μm. (**e**,**f**) Electron dispersive spectroscopy on the selected region of the P3HT:PSS film after 24 h and the P3HT:PSS film after 72 h, respectively. Scale bars, 100 nm.

single unit are almost identical to those of PSS except the presence of oxygen atoms in the former (Fig. 1e). Because the PSS chemically reacts with the P3HT during the TMC formation, we hypothesized that the PSS region might decrease as the TMC-induced fibril nanomorphology developed as a function of time. Indeed, the dark regions were gradually reduced, whereas the evolution of the fibrillar structure was observed in the entire P3HT:PSS film after 48 h. Eventually, the final TMC-induced fibril network nanomorphology on the scale of ~10–20 nm in width and 1–2 μm in length throughout the entire film was formed in the film after 72 h. The sequential change in the nanomorphology of the P3HT:PSS film indicated that the PSS served as a template for forming the TMC-induced fibrillar structure. In addition, because the electron dispersive X-ray spectroscopy line profile on the TMC-induced fibril structure did not show a clear sulphur/oxygen compositional variation (Fig. 1f), we anticipate that the indistinguishable amount of the PSS template may coexist with the P3HT in the fibril structure, which consists of P3HT:PSS.

In contrast to diffraction contrast TEM imaging, which uses coherent elastic scattered electrons, the HAADF-STEM images is obtained from incoherently scattered electrons, which are highly sensitive to variations in the atomic number of atoms and/or relative differences in the electron density of the sample[29]. Thus, the brighter regions in the HAADF-STEM image would be attributed to a relatively higher electron density of the fibrillar structure than that of the surrounding regions. Therefore, we speculate that the TMC-induced fibrillar network nanostructure

(after 72 h, Fig. 1d) could have originated from the P3HT molecules that are highly packed and oriented.

Structural evolution and 3D electrical percolation network. To investigate the improved structural orientation of the P3HT:PSS films, we performed grazing-incidence wide-angle X-ray scattering (GIWAXS) measurements[30–32] on the P3HT and P3HT:PSS films (see Methods for further details). Figure 2a,b present two-dimensional GIWAXS profiles of the pristine P3HT and the P3HT:PSS films. For the pristine P3HT film, two diffusive elliptical-like patterns were observed along the out-of-plane direction at q_z ($Å^{-1}$) = 0.366, which is associated with a lamellar spacing of the (100) plane ($2\pi/0.366 = 17.2$ Å) and at q_z ($Å^{-1}$) = 1.59, which corresponds to the π–π stacking distance of the (010) plane ($2\pi/1.59 = 3.95$ Å). In contrast, the peak associated with the in-plane direction appears at $q_{x,y}$ ($Å^{-1}$) = 0.37, with a weak diffusive elliptical-like pattern. Thus, the weak 'face-on' direction is more favourable in the pristine P3HT film, which implies that lateral charge transport is limited in the pristine P3HT films. For the P3HT:PSS films, however, a series of intense spots appear at the peak positions for the (*h*00) plane along the q_z axis. In addition, an arcing shape for the π–π stacking of the (010) plane along both the q_z axis and the $q_{x,y}$ axis was developed. More importantly, we observed two reverse trends of intensity, one at q_z ($Å^{-1}$) = 0.37 and 1.60 and another at $q_{x,y}$ ($Å^{-1}$) = 0.37 and 1.60, in the one-dimensional scattering profile of the P3HT and the P3HT:PSS films, as shown in Fig. 2c,d, respectively. These results indicate an evolution of the 'edge-on' orientation in the P3HT:PSS films and the overall enhancement of in-plane π–π stacking for the lateral charge transport[33,34].

The relationship between the changed structural formation and the electrical performance for the TMC-induced nanostructure film was investigated using conducting-probe AFM[35,36]. We measured the contact current on the pristine P3HT and P3HT:PSS films by applying a negative bias ($V_{bias} = -5$ V) to a Pt/Cr-coated tip (the Au electrode was grounded). As observed in the topographic images of the two films (Fig. 3a,b), the P3HT:PSS film exhibited a rougher surface morphology with a clearer fibril structure compared with the P3HT film. Surprisingly, these morphological changes are more evident in the current images. In the pristine P3HT film, grain-shaped bright regions (high current) with a diameter that varies between 200 nm and 1 μm were observed. Note that these bright regions are surrounded by dark regions (low current). Thus, it is clear that the lateral charge transport across the entire pristine P3HT film is severely limited by the grain boundary. However, in the P3HT:PSS film, these bright regions are interconnected and spread out throughout the entire film. In addition, the contact current value in the P3HT:PSS film increases by two orders of magnitude compared with that of the pristine P3HT film (see Fig. 3c, the corresponding histograms of the current images of the two films). Because conducting-probe AFM can measure local charge transport in the vertical direction, these results indicate that the vertical charge transports are also enhanced. This observation is consistent with the time-of-flight (ToF) measurements, which are a typical tool used for measuring the vertical transport of semiconductors, on the Indium tin oxide (ITO)/P3HT/Al and ITO/P3HT:PSS/Al device configuration[3,37,38]. The measurement was performed at 532 nm using the frequency-doubled outputs of a Nd:YAG laser (LOTIS). The ToF transients of the P3HT and P3HT:PSS devices were measured at 20–200 V applied biases under pulsed (5 ns) illumination through the ITO electrode. Fig. 3d,e show the typical hole current transient of the P3HT ($t \sim 10$ μm) and P3HT:PSS films ($t \sim 13$ μm) devices recorded at $E = 2.0 \times 10^5$ V cm^{-1} and 1.6×10^4 V cm^{-1}, respectively. The data are plotted on a log–log scale (main plot); the transit time, t_{tr}, is denoted

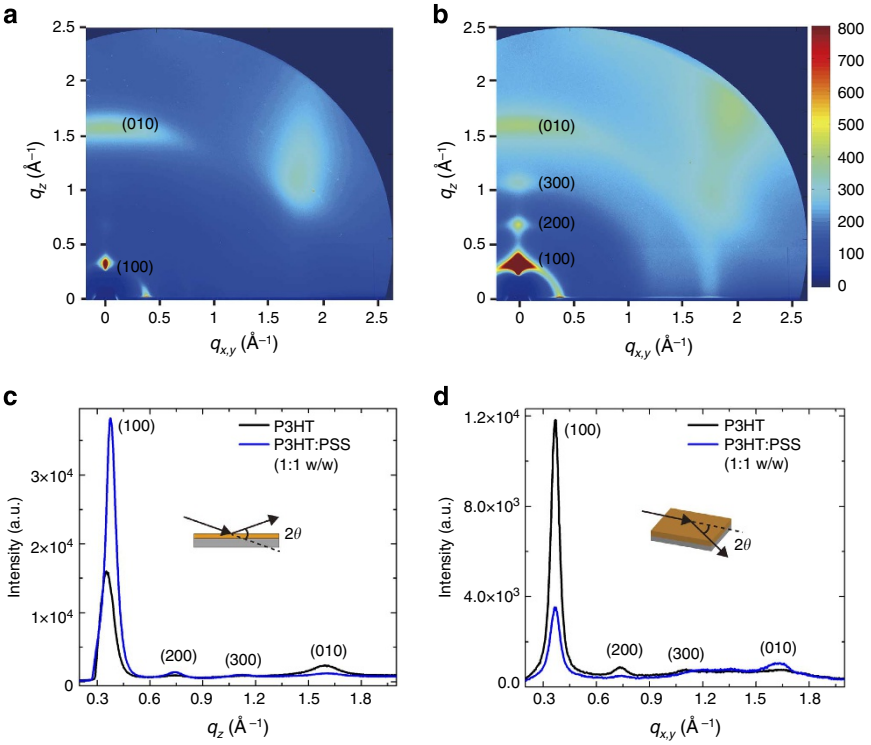

Figure 2 | GIWAXS investigations of P3HT and P3HT:PSS (1:1 w/w) films. (**a**,**b**) Two-dimensional GIWAXS from the pristine P3HT and P3HT:PSS (1:1 w/w) films on a silicon wafer. The incident angle was selected as 0.6°. (**c**,**d**) One-dimensional scattering profiles (out-of-plane and in-plane directions, respectively) obtained from the two-dimensional GIWAXS images. The insets show the incident direction of the X-ray beam.

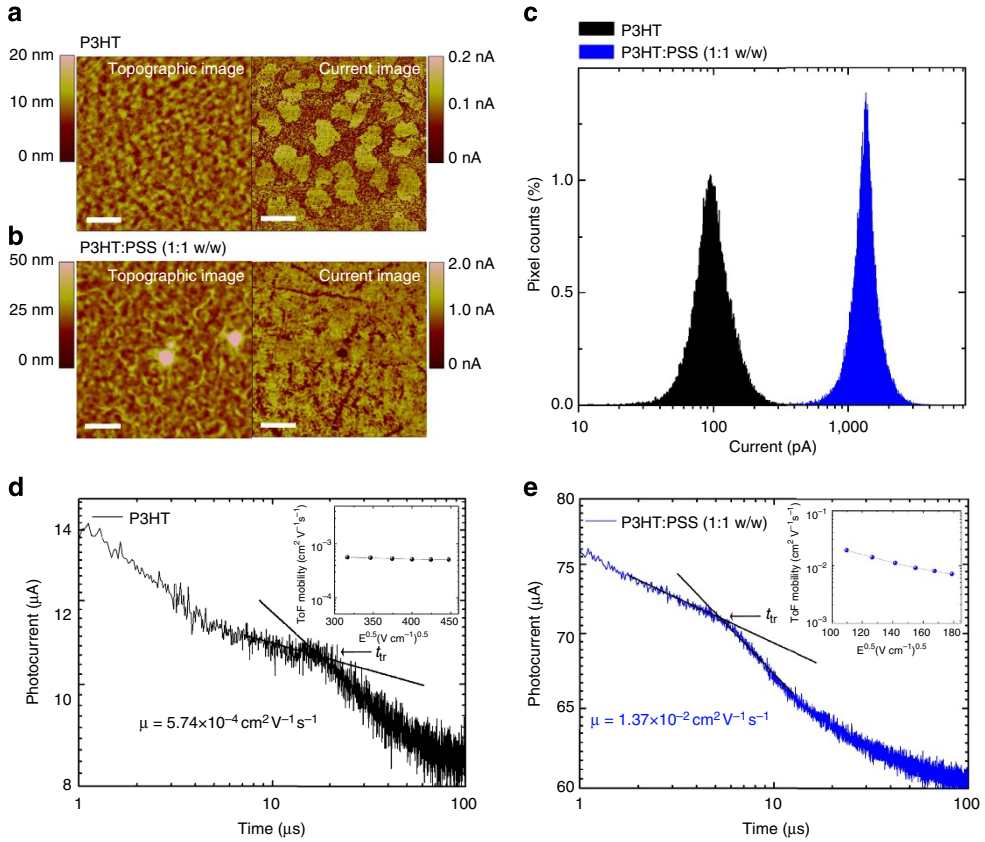

Figure 3 | Relationship between the film morphology and electrical performance. (**a**,**b**) Conducting-probe AFM images of P3HT and P3HT:PSS (1:1 w/w) films. Scale bars, 1 μm. (**c**) Current histograms of P3HT and P3HT:PSS (1:1 w/w) films obtained from the corresponding current image. (**d**,**e**) Transient photocurrent from time-of-flight (ToF) measurements with a device geometry of ITO/P3HT/Al and ITO/P3HT:PSS/Al, respectively. The insets indicate the hole mobility of the corresponding devices plotted as a function of the square root of various bias fields.

with an arrow and is estimated from the intersection point of the log–log plot. The ToF mobility of the P3HT device of $\sim 5 \times 10^{-4}\,cm^2\,V^{-1}\,s^{-1}$ at $E = 2 \times 10^5\,V\,cm^{-1}$ is very similar to that observed in previous studies. However, the ToF mobility in the P3HT:PSS device is remarkably improved by almost two orders of magnitude: $\sim 1.4 \times 10^{-2}\,cm^2\,V^{-1}\,s^{-1}$ at $E = 1.6 \times 10^4\,V\,cm^{-1}$. We also consistently observed the mobility of the P3HT and P3HT:PSS films ($t \sim 130$ nm) in the space-charge-limited current regime (Supplementary Fig. 3 and Supplementary Note 2). Therefore, we concluded that the crystallite-fibril nanostructure and network formation in the P3HT:PSS film induce well-connected, 3D, and isotropic percolation networks for charge transport.

Role of doping and template agents in π-CP films. From a series of optical, structural and electrical experiments on the π-CPs:PSS films, we observed that the acid side-chain group (R-SO_3H) of PSS enables the doping process on π-CP films, whereas the polymer backbone of PSS serves as a structural template for the molecular orientation of π-CPs with a TMC-induced fibril nanostructure. Such bifunctional behaviour of PSS must be related to high-performance electronics of the π-CPs:PSS film. To clarify the relationship between the doping process and the action as a template, we performed experiments using various types of doping/template agents as illustrated in Fig. 4a. We hypothesized that acidic molecular dopants (red panel), such as p-toluene sulphonic acid (TSS) and methanesulfonic acid (MSA), only have a single function of chemical doping on π-CPs (that is, P3HT), whereas non-acidic polymer template agents (green panel), such as poly(sodium 4-styrene sulphonate) (PSS^-:Na^+) and polystyrene (PS), only serve as a template for the molecular orientation of π-CPs. Further information on P3HT:MSA and P3HT:PS films can be found in Supplementary Figs 4 and 5 and Supplementary Table 1.

Figure 4b reveals that distinct ESR signals were observed for the P3HT:TSS and P3HT:PSS films even though no relevant features were observed in the pristine P3HT and P3HT:PSS^-:Na^+ films , implying that the doping process would only be induced by the protonation of acidic dopants. Figure 4c demonstrates the change of charge-carrier density in the corresponding films. The inset presents Mott–Schottky plots (C^{-2} versus V) of the films. As expected, little change was observed in the charge-carrier density for the P3HT:PSS^-:Na^+ film compared with that of the P3HT film ($\sim 2.0 \times 10^{16}\,cm^{-3}$). However, we observed that the P3HT:PSS film was lightly doped to have a charge-carrier density of $4.6 \times 10^{16}\,cm^{-3}$, whereas the P3HT:TSS film was moderately doped to have a charge-carrier density of $2.2 \times 10^{17}\,cm^{-3}$, which is an order of magnitude higher than that of the P3HT film. This behaviour might be interpreted as suggesting the possibility of a light and moderate doping effect on the corresponding transistor performances[39–41]. To verify the doping effect on the transistor performance, the transfer characteristics with a bottom-gate and top-contact transistor configuration ($L = 50\,\mu m$, $W = 1{,}000\,\mu m$) for the corresponding films were determined as shown in Fig. 4d. Although the P3HT:TSS transistor exhibited a field-effect mobility on the order of $\sim 10^{-2}\,cm^2\,V^{-1}\,s^{-1}$ but a reduced

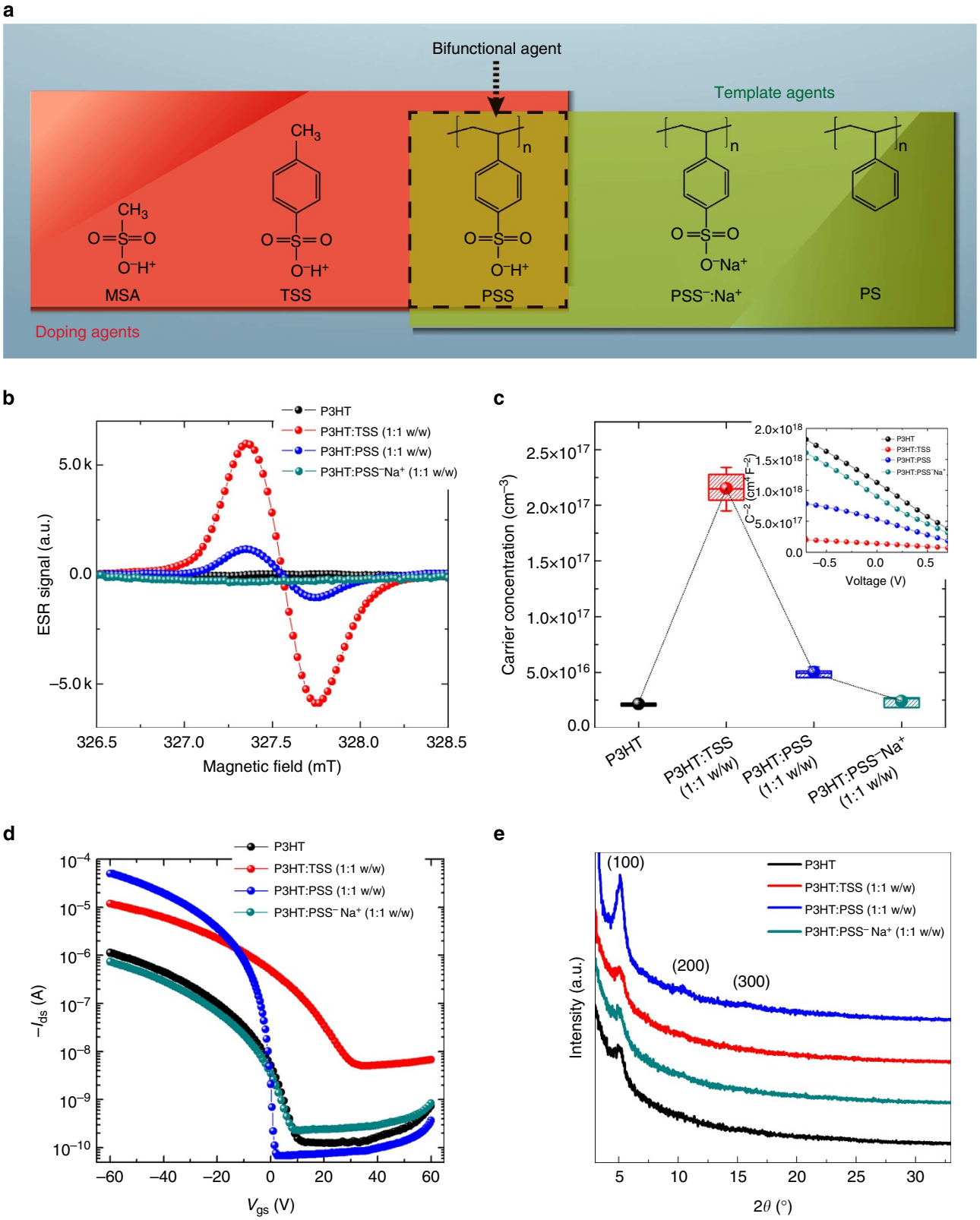

Figure 4 | Role of doping and template agents in π-CP films. (**a**) Schematic diagram of the categorization of doping and template agents depending on their chemical structure. The acidic molecules of MSA and TSS shown in the red panel and the non-acidic polymer of $PSS^-:Na^+$ and PS in the green panel are the doping agents and template agents, respectively; PSS is categorized in the intersection region and is called the bifunctional agent. (**b**) ESR spectra of the pristine P3HT, P3HT:TSS, P3HT:PSS and $P3HT:PSS^-:Na^+$ solutions. (**c**) Plot of charge-carrier density of the corresponding films measured in typical M-I-M configuration, ITO/semiconductor/aluminium. The inset presents a Mott–Schottky plot of the films. The error bars represent standard deviations derived from more than three devices. (**d**) Transfer characteristics of the corresponding PFETs on a Si^{++}/SiO_2 silicon wafer ($t_{ox} \sim 200$ nm); the charge-carrier mobility of the P3HT:TSS film is on the order of $\sim 0.01\,cm^2\,V^{-1}s^{-1}$, whereas the mobility of $P3HT:PSS^-:Na^+$ is on the order of $\sim 0.001\,cm^2\,V^{-1}s^{-1}$. (**e**) High-resolution X-ray diffraction (HR-XRD) patterns of the corresponding films.

on/off ratio ($\sim 10^3$) with the threshold voltage shifting towards positive values, the P3HT:PSS transistor exhibited a high field-effect mobility ($\sim 10^{-1}\,cm^2\,V^{-1}\,s^{-1}$) and a high on-off ratio ($\sim 10^6$) without any threshold shift. This result implied that the light doping process on P3HT would help to extend the electrical connectivity and minimize the trap sites, leading to high-performance electronics[41].

We further noted that the P3HT:TSS film did not exhibit the TMC nanomorphology or the interconnected network that were clearly observed in the P3HT:PSS film, suggesting that the molecular dopant could not serve as a template for the structural orientation (Supplementary Fig. 6). A consistent result was observed in the high-resolution X-ray diffraction spectra of the corresponding films in Fig. 4e. No structural change was observed in either the doped P3HT:TSS film or the undoped P3HT:PSS^-:Na^+ film compared with the P3HT film, whereas a distinct X-ray peak at the (100) plane was observed in the lightly doped P3HT:PSS film. Therefore, by monitoring the change in the charge-carrier density, structural orientation and electrical properties of the P3HT film associated with the various doping/template agent, we concluded that the bifunctional agent (that is, PSS) incorporated with the acid side-chain groups and template polymer backbone would substantially contribute to the light doping process and the structural orientation, thereby leading to a high-performance device exhibiting a high on-current and low off-current.

Hole mobilities in the π-CPs:PSS films at RT. Using a combination of the light doping effect and structural enhancement of π-CPs induced by the bifunctional agent, PSS, we fabricated PFETs to investigate the hole transport characteristics across various π-CPs:PSS films. The PFETs ($L = 50\,\mu m$ and $W = 1{,}000\,\mu m$, defined by a Au source/drain electrode) were fabricated on a heavily n-doped silicon/SiO_2 ($t_{ox} = 200\,nm$) substrate with a bottom-gate and top-contact configuration. Note that the transistors were fabricated without any additional process such as a self-assembled monolayer[9] or high-temperature process ($>150\,°C$)[10], which are typically required for the manipulation of the oriented structure in π-CPs. In Fig. 5a, the pristine P3HT exhibits a relatively low average $\mu_{FET} \approx 8.8 \times 10^{-4}\,cm^2\,V^{-1}\,s^{-1}$ with an on/off ratio of 10^4. However, after the PSS template polymer is added to P3HT, the μ_{FET} value dramatically increases to an average $\mu_{FET} \approx 0.1\,cm^2$

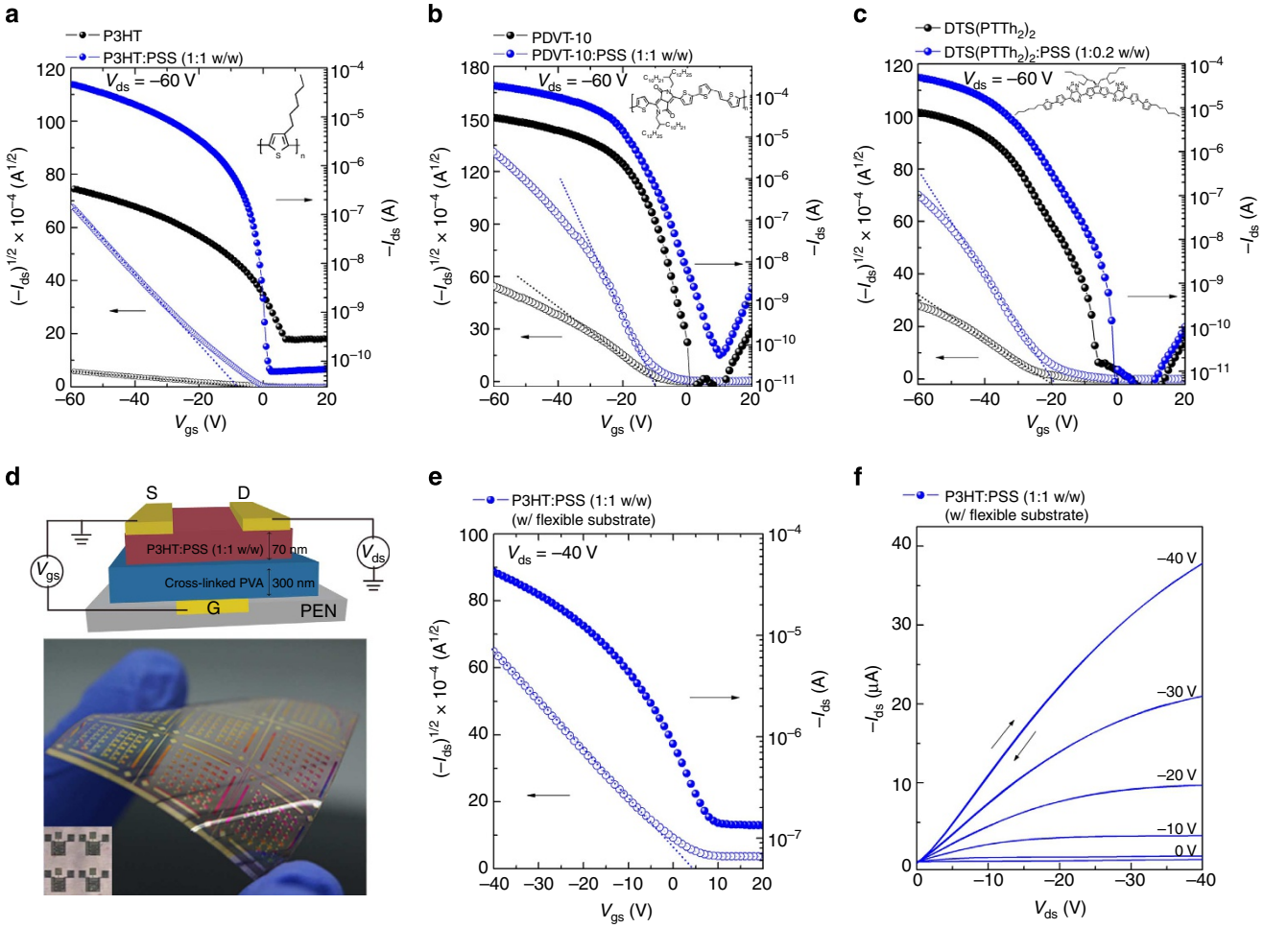

Figure 5 | High-performance OFET devices with various π-CPs:PSS films. (**a**) Transfer characteristics of OFETs on a heavily n-doped Si/SiO_2 silicon wafer ($t_{ox} \sim 200\,nm$) using P3HT semiconductors with and without the PSS template; the OFETs exhibit an improved charge-carrier mobility from $0.0009\,cm^2\,V^{-1}\,s^{-1}$ to $\sim 0.18\,cm^2\,V^{-1}\,s^{-1}$. (**b**,**c**) Transfer characteristics of OFETs on Si^{++}/SiO_2 silicon wafers ($t_{ox} \sim 200\,nm$) using PDVT-10 and $DTS(PTTh_2)_2$ with and without the PSS template; the OFETs exhibit an improved charge-carrier mobility from $0.1\,cm^2\,V^{-1}\,s^{-1}$ to $1.1\,cm^2\,V^{-1}\,s^{-1}$ for PDVT-10 and from $0.03\,cm^2\,V^{-1}\,s^{-1}$ to $0.27\,cm^2\,V^{-1}\,s^{-1}$ for $DTS(PTTh_2)_2$, respectively. The insets show the respective chemical structures. (**d**) The schematic device structure and an image of the corresponding flexible PFETs with an area of $4.4 \times 4.4\,cm^2$ (324 devices). (**e**) Transfer characteristics of the flexible PFET devices with the P3HT:PSS film (1:1 w/w); the devices exhibit a saturation-regime mobility of $\sim 0.25\,cm^2\,V^{-1}\,s^{-1}$. (**f**) Output characteristics of the flexible PFET devices with the P3HT:PSS film (1:1 w/w).

$V^{-1}s^{-1}$ (the maximum $\mu_{FET} \approx 0.18\,cm^2\,V^{-1}\,s^{-1}$) with an on/off ratio of $\sim 10^6$ and an excellent shelf-life stability[41,42] (additional information is provided in Supplementary Figs 7 and 8 and Supplementary Notes 3 and 4). Using the gated transmission line model[43,44], we also observed that the channel resistance of the P3HT:PSS transistor is two orders of magnitude lower than that of the pristine P3HT transistor (Supplementary Fig. 9 and Supplementary Notes 5). We also applied our TMC method to other π-conjugated semiconductors containing a thiophene unit, such as poly[2,5-bis(alkyl)pyrrolo[3,4-c]pyrrole-1,4(2*H*,5*H*)-dione-*alt*-5,5′-di(thiophen-2-yl)-2,2′-(*E*)-2-(2-(thiophen-2-yl)vinyl)thiophene] (PDVT-10) polymers[45] and 5,5′-bis[(4-(7-hexylthiophen-2-yl)thiophen-2-yl)-[1,2,5]thiadiaz-olo[3,4-c]pyridine]-3,3′-di-2-ethylhexylsilylene-2,2′-bithiophene ($DTS(PTTh_2)_2$) small molecules[46,47]. As demonstrated in Fig. 5b, the PDVT-10:PSS (1:1 w/w) transistor exhibits an average mobility of $0.8\,cm^2\,V^{-1}\,s^{-1}$ (the maximum $\mu_{FET} \approx 1.1\,cm^2\,V^{-1}\,s^{-1}$), with a reasonable on/off ratio of $\sim 10^6$, which is an order of magnitude higher than that of the pristine PDVT-10 transistor ($\sim 0.13\,cm^2\,V^{-1}\,s^{-1}$). Similar trends were also observed in the $DTS(PTTh_2)_2$:PSS (1:0.2 w/w) transistor (Fig. 5c); the average mobility increased by an order of magnitude (from $0.03\,cm^2\,V^{-1}\,s^{-1}$ to $0.27\,cm^2\,V^{-1}\,s^{-1}$), with an on/off ratio of $\sim 10^7$ (see Supplementary Fig. 10 for more details). Although the optimized PSS template ratio for the highest device performance was different for each material, we concluded that our PSS template method clearly improves the charge transport of the various π-CPs semiconductors through a combination of the template-mediated structural evolution and light doping effect (Supplementary Figs 11 and 12).

To demonstrate the merits of our TMC method, we successfully produced large-area flexible PFETs fabricated on top of plastic substrates with P3HT:PSS. Figure 5d shows the device configuration and presents an image of the large-area flexible PFET ($4.4 \times 4.4\,cm^2$). As observed in Fig. 5e,f, the flexible PFETs exhibited an average μ_{FET} of $\sim 0.14\,cm^2\,V^{-1}\,s^{-1}$ (the maximum $\mu_{FET} \approx 0.25\,cm^2\,V^{-1}\,s^{-1}$), which is two orders

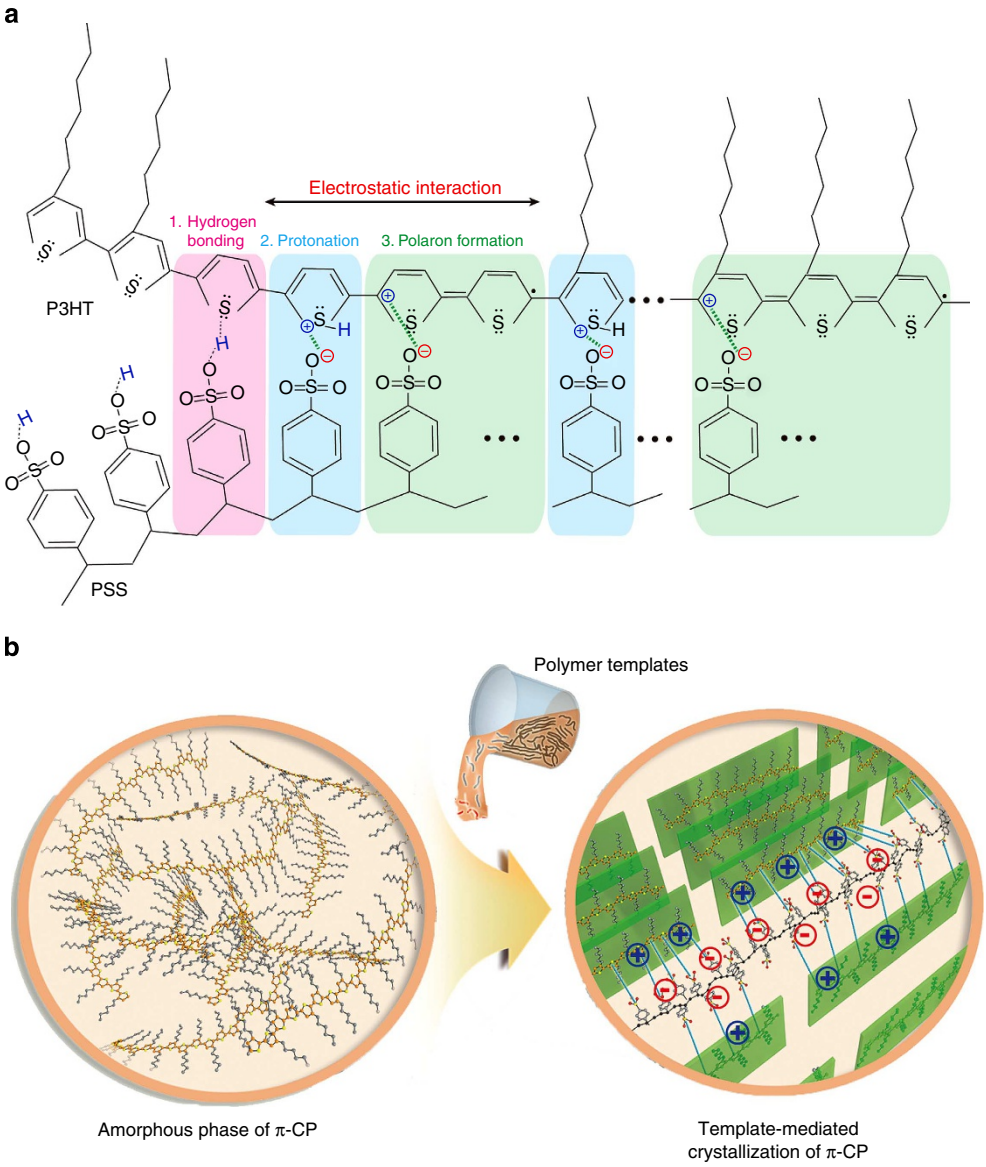

Figure 6 | Mechanism of the formation of TMC-induced fibril nanostructures. (**a**) Detailed mechanism of the electrostatic interaction between π-CPs (that is, P3HT) and the PSS template followed by hydrogen bonding, protonation and polaron formation in the solution state. (**b**) A schematic image of crystallized P3HT molecules along the PSS template via the electrostatic interaction between the P3HT and the template.

of magnitude greater than that of the pristine P3HT ($\sim 0.001\,cm^2\,V^{-1}\,s^{-1}$) and corresponds to the highest μ_{FET} value reported thus far in the devices fabricated on the plastic substrates without any additional steps.

Proposed mechanism for TMC formation in π-CPs:PSS film. Based on our results, the mechanism of light doping and TMC formation in the π-CPs:PSS film (that is, P3HT:PSS) is suggested in Fig. 6a. PSS is a linear polymer with periodically repeating sulphonic acid functional groups, which are deprotonated and carry negative charge (ion). Thus, the ionized PSS can be used as a template to organize the other positively charged polymers (P3HT) via polaron formation and electrostatic interaction between the two materials as follows. (i) Initially, as the two molecules (P3HT and PSS) are close to each other in the organic solution, the hydrogen in the sulphonic acid groups of PSS is bound to a non-bonding electron pair of sulphur (S) atoms in P3HT, forming a R-$SO_3H\cdots S$ hydrogen bond. (ii) The ionized proton (H^+) from PSS is transferred to a non-bonding electron pair of sulphur atoms in the polythiophene to form a sulphur cation, inducing an electrostatic interaction as follows:

$$[\mathrm{P3HT}] + \mathrm{R}-\mathrm{SO_3^-\,H^+} \rightarrow [\mathrm{P3HT:H}]^+ \cdots\cdots \mathrm{R}-\mathrm{SO_3^-}. \quad (1)$$

(iii) The protonated sulphur further changes the electronic structure within the thiophenes and thereby induces a radical cation (spin 1/2) on P3HT ($P3HT^+$) by emitting a hydrogen radical (H), which also induces an electrostatic interaction as follows:

$$2[\mathrm{P3HT}] + 2\mathrm{R}-\mathrm{SO_3^-\,H^+} \rightarrow 2\left([\mathrm{P3HT}]^{+\cdot} \cdots\cdots \mathrm{R}-\mathrm{SO_3^-}\right) + \mathrm{H_2}\uparrow. \quad (2)$$

Critically, the structural repeat of the sulphonic-acid functionalized side-chain group along the single-bond carbon backbone can provide many electrostatic interactions for manipulating the P3HT orientation, which further act as crystal planes for nucleation on which the assembly of neighbouring P3HT molecules is energetically more favourable (Fig. 6b).

Discussion

Using a new TMC method, we succeed in inducing a structural orientation of π-CP along the template polymers over a long range to form an interconnected network throughout the π-CP films without being disconnected by the amorphous regions as in typical π-CPs. This achievement enables 3D isotropic transport with a similar order of improvement along the vertical and lateral directions. By monitoring the experiments with π-CPs and various doping/template agents, we identify that the bifunctional agent, PSS, incorporated in the light doping and template backbone would contribute to the formation of the well-connected nanomorphology of π-CP with TMC structures, leading to high-performance electronics exhibiting high on-currents and on/off ratios.

Although many studies have been conducted on anisotropic alignment systems in π-CPs, our TMC-induced nanomorphology is fundamentally different from the simple chain-ordered structure that relies on the weak interchain interaction between π-CPs. In the TMC system, polymer templates can provide light doping and, as a result, a number of electrostatic interactions with π-CPs for manipulating the π-CP orientation, which enable superior charge transport along the crystallite nano-fibril structure in π-CP films. The achievement of a light doping and network formation of a crystallite nano-fibril structure of π-CPs via such a bifunctional polymer template indicates that a true interconnected pathway of π-CP with a 3D network formation can be prepared from the solution at RT. Because of the superior lateral and vertical charge transport of the TMC-induced π-CP films from the solution at RT, our approach represents an important step towards high-performance printable electronics using plastic substrates.

Methods

Materials. High-purity electronic-grade semiconducting P3HT polymers (~98%) were synthesized by Rieke Metals, MN, USA and were used as received. The regioregularity and average M_w of the P3HT were ~92% and 53 kg mol^{-1}, respectively. The PDVT-10 polymer (average $M_w \approx 50$ kg mol^{-1}) and DTS($PTTh_2$)$_2$ small molecule were purchased from 1-material, Chemscitech Inc., QC, Canada. The insulating PSS template ($M_w \approx 75$ kg mol^{-1}) was purchased from Sigma-Aldrich and was dissolved in 18 wt% H_2O with a pH of 1.55.

Solution preparation. To induce an electrostatic interaction between the semiconductors and the PSS template in solution, we directly added 10 mg of PSS (55.5 mg of the PSS solution) into a 10 mg ml^{-1} π-CP solution that was dissolved in a chloroform solvent. The final weight ratio of the organic semiconductor and the PSS template in the solutions was 1:1. For the DTS($PTTh_2$)$_2$ small molecules, 2 mg of PSS (12 mg of the PSS solution) was introduced into a 10 mg ml^{-1} solution of the small molecules to attain a final weight ratio of 1:0.2. The solutions were subsequently stirred in the dark at RT for more than 72 h and were filtered through a 5-μm polytetrafluoroethylene filter.

Film characterization. Top-down TEM images of the sample films were recorded using a Tecnai G^2 F30 S-Twin microscope operated at an acceleration voltage of 300 kV. The sample films for TEM measurement were obtained by peeling the pre-deposited film ($t \approx 70$ nm) from a glass substrate, and the films were transferred onto 200-mesh copper grids (Electron Microscopy Sciences).

GIWAXS measurements were performed at the 3C-SAXSl beam line in the Pohang Accelerator Laboratory (PAL) using a monochromatized X-ray radiation source of 10.55 eV ($\lambda = 0.117$ nm) and a two-dimensional charge-coupled device (CCD) detector (Mar165 CCD). The samples were mounted on a *z*-axis goniometer equipped with a vacuum chamber (~10^{-3} torr), and the samples were 0.201 m away from the CCD detector. The incident angle of each X-ray beam was set as 0.6°, and the scattering angles were determined from the positions of the reflected X-ray beam from the silicon substrate using pre-calibrated silver beheaded.

Device fabrication and characterization. Before the deposition of the π-CP and π-CP:PSS solutions, heavily n-type-doped silicon substrates covered with 200-nm-thick SiO_2 were solicited with acetone and isopropyl alcohol, respectively, for 10 min and dried at 100 °C for 15 min. The π-CP and π-CP:PSS solutions were deposited onto the substrates at RT and ambient conditions, and the final thickness of the π-CP and π-CP:PSS layers was approximately 70 nm, as measured using a Surf Cored ET 3000. Top-contact and bottom-gate field-effect transistors were finalized with an Au source and drain electrode with a channel length of 50 μm and a width of 1,000 μm. To minimize the effect of environmental conditions, a thin polymethyl methacrylate film ($t \sim 40$ nm) was deposited on the device before the measurement. For the large-area and flexible PFET, a 30-nm-thick aluminium layer was deposited as a gate electrode using a shadow mask on a polyethylene naphthalate substrate (4.4×4.4 cm^2). After spin casting a 5 wt% polyvinyl alcohol (PVA) aqueous solution mixed with ammonium dichromate onto the prepared substrate, we exposed and cross-linked the PVA gate insulator ($\varepsilon \approx 5.4$) using ultraviolet light for 90 s; the final film was rinsed with deionized water. The transfer and output characteristics were determined in a N_2-filled glove box using a Keithley 4200 source metre (internal impedance > 10^{10} Ω). The saturation-regime mobility of the transistor was determined using the following equation: $I_{ds} = (WC_i/2L)\,\mu_{sat}(V_g - V_{th})^2$, where I_{ds} is the source-drain current, C_i (17.2 nF cm^{-2}) is the capacitance per unit area, L is the channel length, W is the channel width, μ_{sat} is the saturation-regime charge carrier mobility and V_g and V_{th} are the gate and threshold voltages, respectively.

References

1. Forrest, S. R. The path to ubiquitous and low-cost organic electronic appliances on plastic. *Nature* **428,** 911–918 (2004).
2. Klauk, H. Plastic electronics: Remotely powered by printing. *Nat. Mater.* **6,** 397–398 (2007).
3. Yasuhiko, S. & Hiroshi, K. Charge carrier transporting molecular materials and their applications in devices. *Chem. Rev.* **107,** 953–1010 (2007).
4. Facchetti, F. π-Conjugated polymers for organic electronics and photovoltaic cell applications. *Chem. Mater.* **23,** 733–758 (2011).
5. Street, R. A., Northrup, J. E. & Salleo, A. Transport in polycrystalline polymer thin-film transistors. *Phys. Rev. Lett.* **71,** 165202 (2005).
6. Kline, R. J. *et al.* Dependence of regioregular poly(3-hexylthiophene) film morphology and field-effect mobility on molecular weight. *Macromolecules* **38,** 3312–3319 (2005).

7. Rivnay, J. *et al.* Large modulation of carrier transport by grain-boundary molecular packing and microstructure in organic thin films. *Nat. Mater.* **8,** 952–958 (2009).
8. Noriega, R. *et al.* A general relationship between disorder, aggregation and charge transport in conjugated polymers. *Nat. Mater.* **12,** 1038–1044 (2013).
9. Kline, R. J., McGehee, M. D. & Toney, M. F. Highly oriented crystals at the buried interface in polythiophene thin-film transistors. *Nat. Mater.* **5,** 222–228 (2006).
10. McCulloch, I. *et al.* Liquid-crystalline semiconducting polymers with high charge-carrier mobility. *Nat. Mater.* **5,** 328–333 (2006).
11. Tseng, H. *et al.* High mobility field effect transistors based on macroscopically oriented regioregular copolymers. *Nano Lett.* **12,** 6353–6357 (2012).
12. Diao, Y. *et al.* Solution coating of large-area organic semiconductor thin films with aligned single-crystalline domains. *Nat. Mater.* **12,** 665–671 (2013).
13. Kim, B. *et al.* A molecular design principle of lyotropic liquid-crystalline conjugated polymers with directed alignment capability for plastic electronics. *Nat. Mater.* **12,** 659–664 (2013).
14. Heil, H. *et al.* The influence of mechanical rubbing on the field-effect mobility in polyhexylthiophene. *J. Appl. Phys.* **93,** 1636–1641 (2003).
15. Yang, C. Y., Soci, C., Mosesa, D. & Heeger, A. J. Aligned rrP3HT film: Structural order and transport properties. *Synt. Met.* **155,** 639–642 (2005).
16. Brinkmann, M. & Rannou, P. Effect of molecular weight on the structure and morphology of oriented thin films of regioregular poly(3-hexylthiophene) grown by directional epitaxial solidification. *Adv. Funct. Mater.* **17,** 101–108 (2007).
17. Sirringhaus, H. *et al.* Mobility enhancement in conjugated polymer field-effect transistors through chain alignment in a liquid-crystalline phase. *Appl. Phys. Lett.* **77,** 406–408 (2000).
18. van de Craats, A. M. *et al.* Meso-epitaxial solution-growth of self-organizing discotic liquid-crystalline semiconductors. *Adv. Mater.* **15,** 495–499 (2003).
19. Yu, G., Gao, J., Hummelen, J. C., Wudl, F. & Heeger, A. J. Polymer photovoltaic cells: enhanced efficiencies via a network of internal donor-acceptor heterojunctions. *Science* **270,** 1789–1791 (1995).
20. Burroughes, J. H. *et al.* Light-emitting diodes based on conjugated polymers. *Nature* **347,** 539–541 (1990).
21. Kirchmeyer, S. & Reuter, K. Scientific importance, properties and growing applications of poly(3,4-ethylenedioxythiophene). *J. Mater. Chem.* **15,** 2077–2088 (2005).
22. Chen, T., Wu, X. & Rieke, R. D. Regiocontrolled synthesis of poly(3-alkylthiophenes) mediated by Rieke Zinc: their characterization and solid-state properties. *J. Am. Chem. Soc.* **117,** 233–244 (1995).
23. Bao, Z., Dodabalapur, A. & Lovinger, A. J. Soluble and processable regioregular poly(3-hexylthiophene) for thin film field-effect transistor applications with high mobility. *Appl. Phys. Lett.* **69,** 4108–4110 (1996).
24. Brown, P. J. *et al.* Effect of interchain interactions on the absorption and emission of poly(3-hexylthiophene). *Phys. Rev. B* **67,** 64203 (2003).
25. Patil, A. O., Heeger, A. J. & Wudl, F. Optical properties of conducting polymers. *Chem. Rev.* **88,** 183–200 (1988).
26. Österbacka, R., An, C. P., Jiang, X. M. & Vardeny, Z. V. Two-dimensional electronic excitations in self-assembled conjugated polymer nanocrystals. *Science* **287,** 839–842 (2000).
27. Yoo, J. E. *et al.* Directly patternable, highly conducting polymers for broad applications in organic electronics. *Proc. Natl Acad. Sci. USA* **107,** 5712–5717 (2010).
28. Shrotriya, V. *et al.* Absorption spectra modification in poly(3-hexylthiophene): methanofullerene blend thin films. *Chem. Phys. Lett.* **411,** 138–143 (2005).
29. Williams, D. B. & Carter, C. B. in: *Transmission Electron Microscopy: a textbook for materials science. Part 3: Imaging*. **Ch. 22**, 371–381 (Springer, 2009).
30. Sirringhaus, H. *et al.* Two-dimensional charge transport in self-organized, high-mobility conjugated polymers. *Nature* **401,** 685–688 (1999).
31. Yang, H. *et al.* Effect of mesoscale crystalline structure on the field-effect mobility of regioregular poly(3-hexyl thiophene) in thin-film transistors. *Adv. Funct. Mater.* **15,** 671–676 (2005).
32. DeLongchamp, D. M. *et al.* Molecular characterization of organic electronic films. *Adv. Mater.* **23,** 319–337 (2011).
33. Kline, R. J. *et al.* Significant dependence of morphology and charge carrier mobility on substrate surface chemistry in high performance polythiophene semiconductor films. *Appl. Phys. Lett.* **90,** 062117 (2007).
34. Salleo, A. Charge transport in polymeric transistors. *Mater. Today* **10,** 38–45 (2007).
35. Yang, S. Y. *et al.* Enhanced electrical percolation due to interconnection of three-dimensional pentacene islands in thin films on low surface energy polyimide gate dielectrics. *J. Phys. Chem. B* **110,** 20302–20307 (2006).
36. Kim, J. S. *et al.* Poly(3-hexylthiophene) nanorods with aligned chain orientation for organic photovoltaics. *Adv. Funct. Mater.* **20,** 540–545 (2010).
37. Choulis, S. A. *et al.* High ambipolar and balanced carrier mobility in regioregular poly(3-hexylthiophene). *Appl. Phys. Lett.* **85,** 3890–3892 (2004).
38. Huang, J., Li, G. & Yang, Y. Influence of composition and heat-treatment on the charge transport properties of poly(3-hexylthiophene) and [6,6]-phenyl C61-butyric acid methyl ester blends. *Appl. Phys. Lett.* **87,** 112105 (2005).
39. Pingel, P. *et al.* Charge-transfer localization in molecularly doped thiophene-based donor polymers. *J. Phys. Chem. Lett.* **1,** 2037–2041 (2010).
40. Pingel, P., Schwarzl, R. & Neher, D. Effect of molecular p-doping on hole density and mobility in poly(3-hexylthiophene). *Appl. Phys. Lett.* **100,** 143303 (2012).
41. Lu, G. *et al.* Moderate doping leads to high performance of semiconductor/insulator polymer blend transistors. *Nat. Commun.* **4,** 1588 (2013).
42. Arias, A. C., Endicott, F. & Street, R. A. Surface-Induced self-encapsulation of polymer thin-film transistors. *Adv. Mater.* **18,** 2900–2904 (2006).
43. Hamadani, B. H., Gundlach, D. J., McCulloch, I. & Heeney, M. Undoped polythiophene field-effect transistors with mobility of $1\,cm^2\,V^{-1}\,s^{-1}$. *Appl. Phys. Lett.* **91,** 243512–243513 (2007).
44. Wang, S. D., Yan, Y. & Tsukagoshi, K. Understanding contact behavior in organic thin film transistors. *Appl. Phys. Lett.* **97,** 63307 (2010).
45. Chen, H. *et al.* Highly π-extended copolymers with diketopyrrolopyrrole moieties for high-performance field-effect transistors. *Adv. Mater.* **24,** 4618–4622 (2012).
46. Sun, Y. *et al.* Solution-processed small-molecule solar cells with 6.7% efficiency. *Nat. Mater.* **11,** 44–48 (2012).
47. Zhong, C., Huang, F., Cao, Y., Moses, D. & Heeger, A. J. Role of localized states on carrier transport in bulk heterojunction materials comprised of organic small molecule donors. *Adv. Mater.* **26,** 2341–2345 (2014).

Acknowledgements

We thank the Heeger Center for Advanced Materials (HCAM) and the Research Institute of Solar & Sustainable Energies (RISE) at the Gwangju Institute of Science and Technology (GIST) of Korea for assistance with the device fabrication and characterization. K.L. also acknowledges support from the National Research Foundation of Korea (NRF) grant funded by the Korean government (MSIP) (No. 2008-0062606, CELA-NCRC).

Author contributions

S.K., K.K. and K.L. designed the concept and the required experiments. S.K., K.Y. and K.K. set up and conducted the experiments. Y.R.J. and B.J.K. performed the TEM measurements, with S.K. fabricating the samples. S.K., K.Y. and J.K. performed the GIWAXS measurements. S.K., K.Y., G.K., H.K. and K.L. interpreted the data and wrote the manuscript.

Additional information

Supplementary Information accompanies this paper at http://www.nature.com/naturecommunications

Competing financial interests: The authors declare no competing financial interests.

Reprints and permission information is available online at http://npg.nature.com/reprintsandpermissions/

How to cite this article: Kwon, S. *et al.* Template-mediated nano-crystallite networks in semiconducting polymers. *Nat. Commun.* 5:4183 doi: 10.1038/ncomms5183 (2014).